machines

Article

Novel Feature Extraction and Locomotion Mode Classification Using Intelligent Lower-Limb Prosthesis

Yi Liu, Honglei An *, Hongxu Ma and Qing Wei

College of Intelligence Science and Technology, National University of Defense Technology, Changsha 410073, China
* Correspondence: eric_hong@nudt.edu.cn

Abstract: Intelligent lower-limb prosthesis appears in the public view due to its attractive and potential functions, which can help amputees restore mobility and return to normal life. To realize the natural transition of locomotion modes, locomotion mode classification is the top priority. There are mainly five steady-state and periodic motions, including LW (level walking), SA (stair ascent), SD (stair descent), RA (ramp ascent), and RD (ramp descent), while ST (standing) can also be regarded as one locomotion mode (at the start or end of walking). This paper mainly proposes four novel features, including TPDS (thigh phase diagram shape), KAT (knee angle trajectory), CPO (center position offset) and GRFPV (ground reaction force peak value) and designs ST classifier and artificial neural network (ANN) classifier by using a user-dependent dataset to classify six locomotion modes. Gaussian distributions are applied in those features to simulate the uncertainty and change of human gaits. An angular velocity threshold and GRFPV feature are used in the ST classifier, and the artificial neural network (ANN) classifier explores the mapping relation between our features and the locomotion modes. The results show that the proposed method can reach a high accuracy of 99.16% ± 0.38%. The proposed method can provide accurate motion intent of amputees to the controller and greatly improve the safety performance of intelligent lower-limb prostheses. The simple structure of ANN applied in this paper makes adaptive online learning algorithms possible in the future.

Keywords: phase variable; prosthesis; mode classification; feature; steady states; accuracy

Citation: Liu, Y.; An, H.; Ma, H.; Wei, Q. Novel Feature Extraction and Locomotion Mode Classification Using Intelligent Lower-Limb Prosthesis. *Machines* **2023**, *11*, 235. https://doi.org/10.3390/machines11020235

Academic Editors: Yassine Bouteraa, Imdad Ullah and Ben Abdallah Ismail

Received: 15 January 2023
Revised: 27 January 2023
Accepted: 1 February 2023
Published: 5 February 2023

1. Introduction

According to the statistics of the World Health Organization (WHO), about 15% (975 million) of the world's population have physical disabilities to varying degrees [1]. Some of them suffer from lower-limb amputation (LLA). For people with LLA, lower limb prosthesis is an important tool to help them restore mobility and live a better life. However, at present, the majority of commercial prosthetic legs are passive, and walking with them will consume 20~30% more energy than healthy individuals [2]. Moreover, the obvious asymmetry between the sound side and the affected side will lead to secondary damage. When people with LLA are in a complex walking environment, even stability will become a luxury [3]. Research on intelligent lower-limb prostheses has been performed recently due to their adaptation in different terrains.

The common control framework of intelligent lower-limb prostheses is a hierarchical control system [4] shown in Figure 1. The high-level controller focuses on human intent recognition to distinguish locomotion modes in real time and obtain gait parameters and gait phase, which will be sent to the middle-level controller to compute desired joint angles and torques. The low-level controller aims at making the actuators output the desired torques. In this paper, we focus on locomotion mode classification, which belongs to the high-level controller of the prosthesis control system.

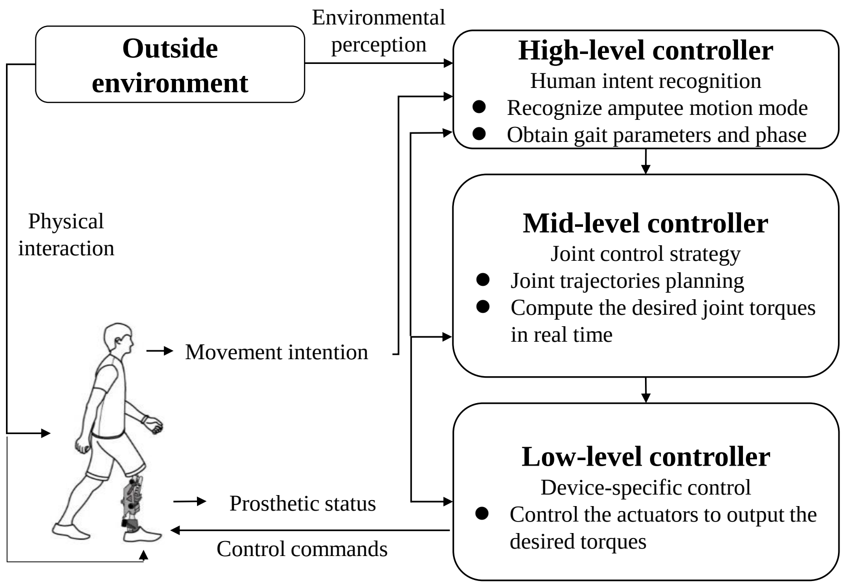

Figure 1. The hierarchical control system [4] of intelligent powered low limb prosthesis based on the gait phase.

Pattern recognition (PR), machine learning (ML), and statistical methods have been widely applied to classify locomotion modes from surface electromyogram (sEMG) signals [5] to mechanical sensors. Ref. [6] collects sEMG signals to interpret motion modes. J A Spanias et al. developed an adaptive PR system to adapt to changes in the user's neural information during ambulation and consistently identify the user's intent over multiple days with a classification accuracy of 96.31% $\pm$ 0.91% [7]. Zhang et al. present a robust environmental feature recognition system (EFRS) to predict the locomotion modes of amputees and estimate environmental features with the depth camera [8]. Ref. [9] combines EMG and mechanical sensors, using linear discriminant analysis (LDA) to reach 86% accuracy. Quadratic discriminant analysis (QDA) in [10] gets a similar result with EMG only. Ref. [11] infers the user's intent with the Gaussian mixture model (GMM). They combine foot force and EMG to distinguish intent to stand, sit and walk. Ref. [12] combines all sensors to recognize six locomotion modes and five mode transitions by support vector machine (SVM) and gets a high accuracy of 95%. Ref. [13] adopts dynamic Bayesian network (DBN) to recognize level walking (LW), stair ascent (SA), stair descent (SD), ramp ascent (RA) and ramp descent (RD) with a load cell and a six-axis inertial measurement unit (IMU). Ref. [14] depends only on ground reaction force (GRF) to distinguish LW and SD by an artificial neural network (ANN). Recently, [15] encodes data from IMUs into picture format and inputs this 2D image into a convolutional neural network (CNN). The CNN outputs the probability of five steady states and eight transition states. They successfully improve the accuracy to 95.8%. Similarly, Kang et al. developed a DL-based (deep learning-based) classifier for five steady states, which is user-independent and achieved an overall accuracy of 98.84% $\pm$ 0.47% [16]. Ref. [17] uses ML methods to compare the user-independent and dependent intent recognition systems for powered prostheses. The results show that the user-dependent method has better accuracy. The previous works have achieved good results in locomotion mode classification. However, the traditional extracted features are generally the average, maximum, minimum, median and variance of sensors' data, which lack a physical explanation. The DL methods need big data collection, which is unfriendly to the amputees.

Based on 2 IMUs (Placed on the thigh and shank of amputees' sound leg, respectively) and a GRF insole (Placed in the amputees' sound leg's shoe), shown in Figure 2, which are used to collect a user-dependent dataset, this paper extracts four novel features and design classifiers to recognize locomotion modes. The main contributions of this paper are as follows: (1) based on the processed sensor data, four novel features are extracted; (2) the fluctuation of gait data is expressed by Gaussian distributions to simulate the fluctuation of human motion trajectory; (3) The designed classifiers achieve a higher accuracy of 99.16% ± 0.38% compared with previous works.

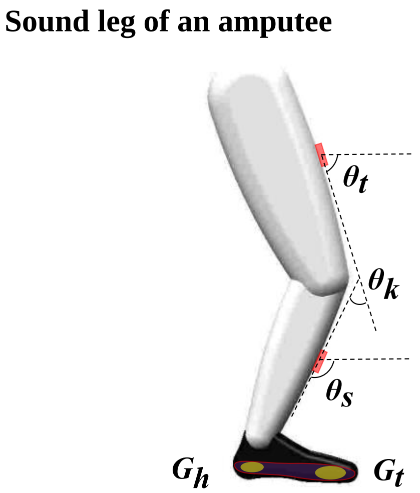

Figure 2. Sensor installation positions and variable descriptions. Θ_t is the thigh IMU angle in the sagittal plane, θ_s is the shank IMU angle in the sagittal plane and θ_k is the knee angle. G_h and G_t are the raw force sensor data of the heel and toe.

2. Materials and Methods

2.1. Data Acquisition and Processing

2.1.1. Data Collection

Eight able-bodied subjects agreed to participate in the data acquisition experiments, including six males (varies in height (1.63–1.81 m) and weight (58–76 kg)) and two females (varies in height (1.65–1.7 m) and weight (50–55 kg)). They are required to equip with an intelligent prosthesis in Figure 3a. The intelligent lower-limb prosthesis is designed for healthy individuals in which the knee and ankle are active joints that provide power in the sagittal plane. The finite state machine impedance control [18] is applied for the intelligent prosthesis, and the joint torques τ_i are determined according to Equation (1)

$$\tau_i = k_i(\theta_i - \theta_{eqi}) + b_i\dot{\theta}_i \tag{1}$$

where i denotes the prosthesis knee or ankle, θ is the joint angle and $\dot{\theta}$ is the joint angular velocity. K, b and θ_e are the stiffness, damping and equilibrium positions, respectively, and are assigned different values under different states and locomotion modes. The impedance parameters are set to make the subject walk comfortably.

Moreover, data acquisition sensors, including IMUs and GRF insoles, are set, as shown in Figure 3b. IMU data consist of angle and angular velocity in the x, y, and z-axis directions, respectively, with a sampling frequency of 100 Hz. The GRF insoles measure pressure in the vertical direction with a frequency of 100 Hz.

This paper aims to classify 6 locomotion modes, shown in Figure 4, and the locomotion settings, including an incline-adjustable treadmill and 2 stairs of different heights, are shown in Figure 5. The ramp inclines are set to ±3.6°, ±5.8° and ±9.5°. Under each incline, subjects walk for 30 s with low, normal and fast speeds (0.56 m/s, 0.83 m/s and 1.11 m/s). To keep the data sizes in different modes almost the same, each subject walks on the level ground (LG) for 90 s at each speed. As for SA and SD, subjects completed 10 trials under different stair heights of 11.8 cm and 14.5 cm. Finally, subjects maintain a relaxing standing posture on level ground for 60 s.

(**a**) (**b**)

Figure 3. (**a**) Intelligent lower-limb prosthesis designed for able-bodied subjects. (**b**) The able-bodied subject equipped with a prosthesis and data acquisition sensors.

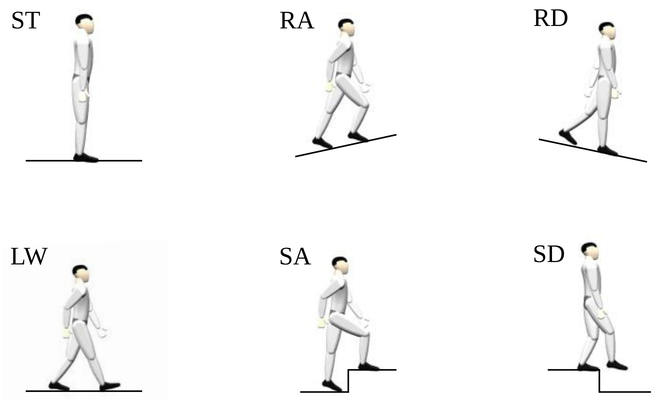

Figure 4. Six locomotion modes including level walking (LW), stair ascent (SA), stair descent (SD), ramp ascent (RA), ramp descent (RD), and standing (ST).

(**a**) (**b**) (**c**)

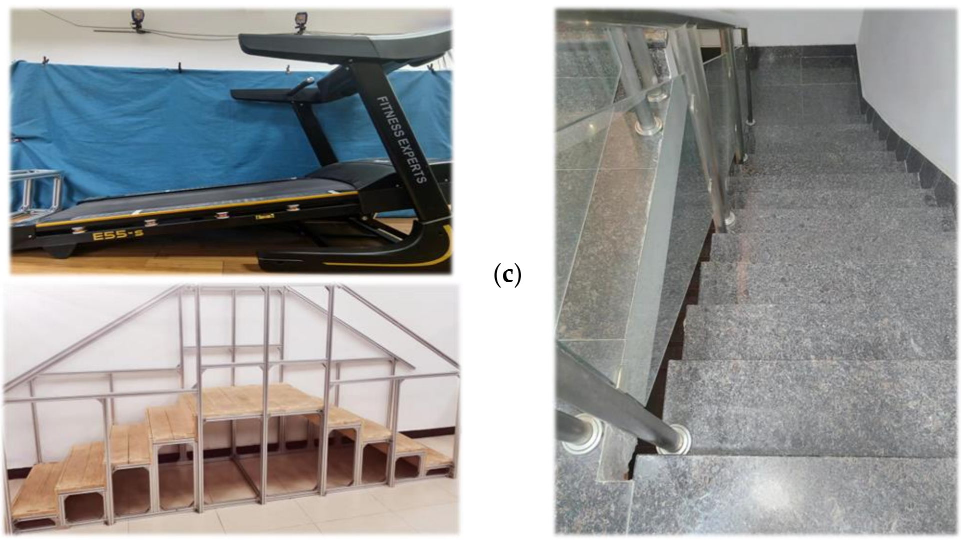

Figure 5. (**a**) Incline adjustable treadmill. (**b**) Stairs with 14.5 cm stair height. (**c**) Stairs with 11.8 cm stair height.

Our final dataset includes data from 3 sensors: 2 IMUs placed at the thigh and the shank of the sound leg and a GRF insole put in the shoe on the same side (Figure 2). We only used IMU data in the sagittal plane direction. The raw sensor dataset under ω_m mode is recorded as follows:

$$D_{\omega_m}^{raw} = \{(\theta_t, \dot{\theta}_t, \theta_s, G_h, G_t)|\omega_m\} \tag{2}$$

For clarity, we list some parameters in Table 1 below and some abbreviations in Table A1 of Appendix A.

Table 1. Variable descriptions.

Symbol	Quantity
M	Total number of modes except for ST ($M = 5$)
$\dot{\theta}_t$	Thigh IMU angular velocity in the sagittal plane
ω_m	Locomotion mode. $\omega_m \in \{\text{LW}, \text{SA}, \text{SD}, \text{RA}, \text{RD}, \text{ST}\}$
t_s	The sampling period and $t_s = 0.01$s
L_{tw}	The length of the time window.

2.1.2. Gait Phase Variable

There are experiments using motion capture systems that prove that the human thigh motion can uniquely and continuously represent the gait cycle [19]. The continuous gait phase variable is defined by the atan2 function:

$$\varphi(t) = \text{atan2}(\dot{\theta}_t, \theta_t) + \pi \tag{3}$$

However, there are noises and ground impact in thigh angular velocity $\dot{\theta}_t$. The linear polynomial fitting method is adopted to smooth the $\dot{\theta}_t(t)$ curve, as shown in Figure 6a.

$$\dot{\theta}_{t\_s}(t) = (1-r)\dot{\theta}_t(t) + r \cdot [a(t) \cdot t + b(t)] \tag{4}$$

where $a(t)$ and $b(t)$ are linear fitting parameters calculated by the least square method online according to Equation (5), and r is the smoothing coefficient. In Equation (5), n is the sample number. Here, $n = 40$ and $r = 0.9$.

$$\begin{gathered} a(t) = [\sum_{k=1}^{n}(t-k \cdot t_s) \cdot \dot{\theta}_t(t-k \cdot t_s) - n\overline{x}\overline{y}]/[\sum_{k=1}^{n}(t-k \cdot t_s)^2 - n\overline{x}^2] \\ \overline{x} = \sum_{k=1}^{n}(t-k \cdot t_s)/n, \overline{y} = \sum_{k=1}^{n}\dot{\theta}_t(t-k \cdot t_s)/n \\ b(t) = \overline{y} - a(t) \cdot \overline{x} \end{gathered} \tag{5}$$

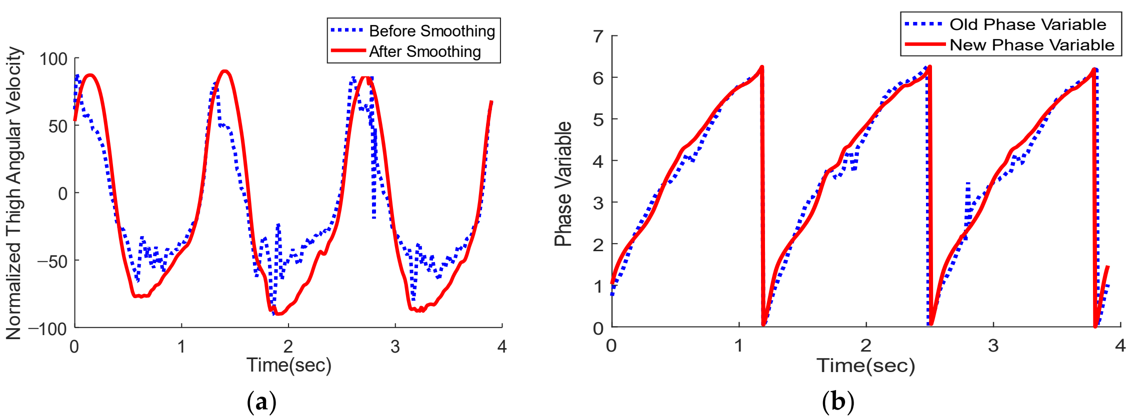

Figure 6. (**a**) Smoothing effect on the normalized thigh Angular velocity. (**b**) The new gait phase variable shows better monotonicity at the time axis.

By translation, the phase diagram trajectory can wrap the origin and make the phase variable vary circularly. By normalization, we can obtain a similar phase diagram trajectory under the same locomotion mode with different walking speeds. The transformation formulas [19] are as follows:

$$\theta_{t\_tn}(t) = \alpha_x(t)[\theta_t(t) + \beta_x(t)]\gamma \quad \dot{\theta}_{t\_stn}(t) = \alpha_y(t)[\dot{\theta}_{t\_s}(t) + \beta_y(t)]\gamma \tag{6}$$

where $\gamma = 180$ is the scale factor, $\alpha(t)$ is the normalization factor, and $\beta(t)$ is the translation factor which can be calculated by:

$$\begin{aligned} \alpha_x(t) &= \frac{1}{|\max[\theta_t(t)] - \min[\theta_t(t)]|}, \alpha_y(t) = \frac{1}{\left|\max[\dot{\theta}_{t\_s}(t)] - \min[\dot{\theta}_{t\_s}(t)]\right|}, \\ \beta_x(t) &= \frac{-|\max[\theta_t(t)] + \min[\theta_t(t)]|}{2}, \beta_y(t) = \frac{-\left|\max[\dot{\theta}_{t\_s}(t)] + \min[\dot{\theta}_{t\_s}(t)]\right|}{2}. \end{aligned} \tag{7}$$

Data of the previous gait cycle from moment t are taken to calculate the maximum and minimum in real time. The new continuous gait phase variable (Figure 6b) is defined as

$$\varphi_{new}(t) = \text{atan2}\left[\dot{\theta}_{t\_stn}(t), \theta_{t\_tn}(t)\right] + \pi \tag{8}$$

2.1.3. Knee Angle and GRF value

The knee angle is calculated as:

$$\theta_k = \theta_s - \theta_t \tag{9}$$

The smoothing method in Equation (4) ($n = 20$ and $r = 0.9$) is applied at the knee angle to get a smoother curve $\theta_{k\_s}(t)$. To obtain similar knee trajectory under the same locomotion mode with different walking speeds, $\theta_{k\_s}(t)$ is normalized to $\theta_{k\_sn}(t)$.

The GRF of the heel and toe are recorded as $G_h(t)$ and $G_t(t)$ respectively. Their latest peak values are recorded as $G_{hp}(t)$ and $G_{tp}(t)$ during one gait cycle before.

Then, the processed dataset D_{ω_m} is

$$D_{\omega_m} = \left\{ (\theta_{t\_tn}, \dot{\theta}_{t\_stn}, \varphi_{new}, \theta_{k\_sn}, \beta_x, \beta_y, G_{tp}, G_{hp}) \middle| \omega_m \right\} \tag{10}$$

$[0, 2\pi)$ is discretized into f_p parts of the same length according to Equation (11).

$$\varphi_j = [\frac{2\pi j}{f_p}, \frac{2\pi(j+1)}{f_p})(j = 0, 1, 2, \ldots, f_p - 1) \tag{11}$$

D_{ω_m} is divided into D_{ω_m,φ_j} according to which part φ_{new} belongs to. The divided datasets are used to calculate feature distributions under different modes. The workflow of offline data processing and feature distribution calculation are shown in Figure 7.

2.2. Feature Distributions and Extractions

2.2.1. Thigh Phase Diagram Shape (TPDS)

The thigh phase diagram consists of processed thigh IMU angle θ_{t_sn} in the x-axis and processed thigh IMU angular velocity $\dot{\theta}_{t\_stn}$ in y-axis. The trajectory of $\left(\theta_{t\_tn}, \dot{\theta}_{t\_stn}\right)$ during walking is named TDPS, and TDPS varies from each other under different locomotion modes. Here, Gaussian distributions are used to record the standard TDPS of different locomotion modes. For example, the TPDS under LW mode is shown in Figure 8a.

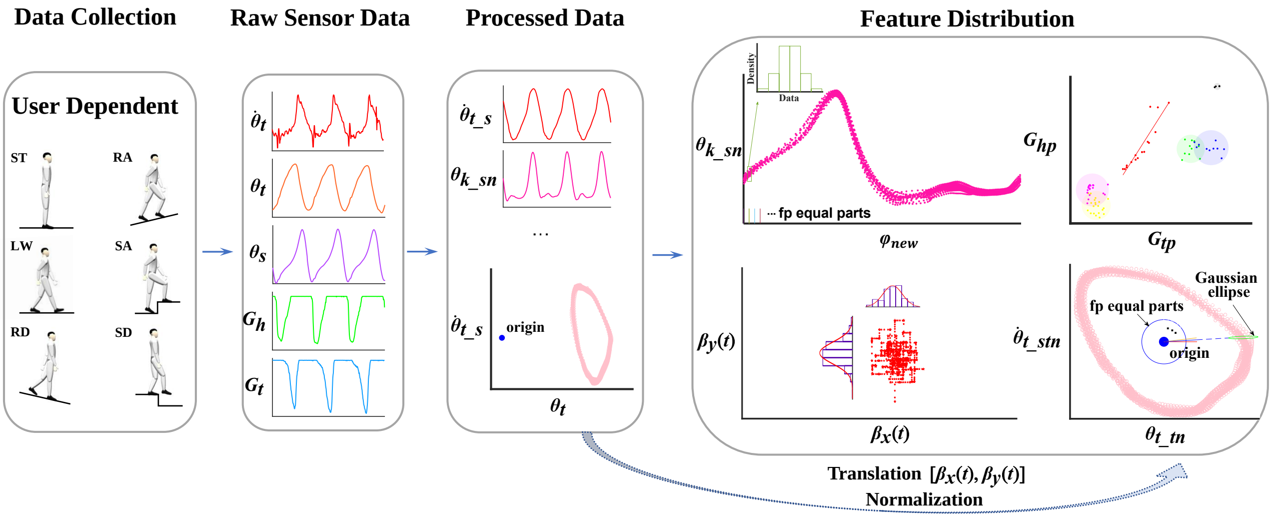

Figure 7. Offline data processing and feature distribution calculation.

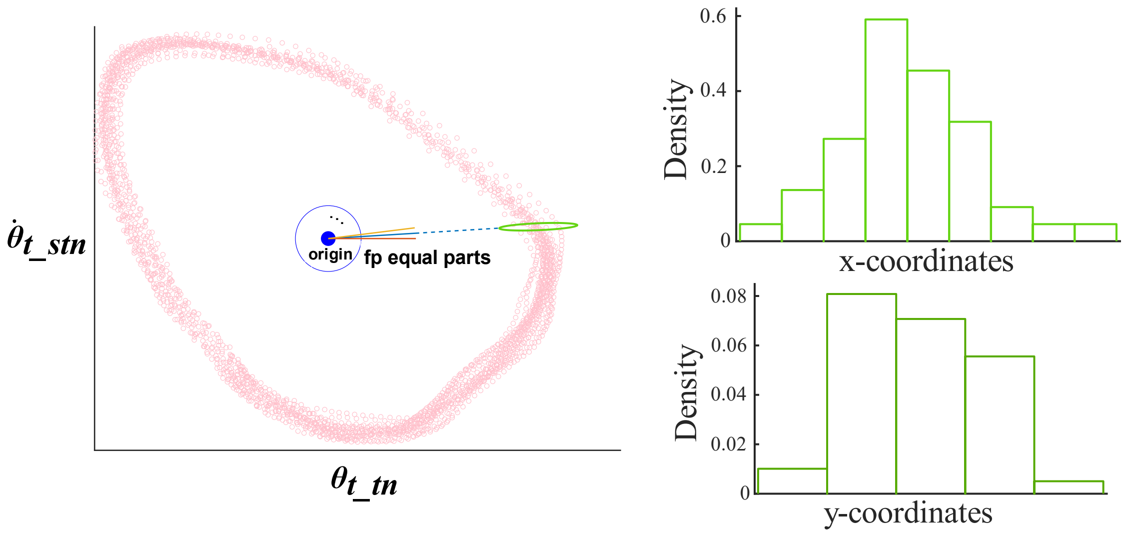

(**a**) (**b**)

Figure 8. (**a**) TPDS of LW mode. Pink points belong to the dataset D_{LW}. Points in the green circle are in the dataset D_{LW,φ_0}. (**b**) The distributions of x-coordinates and y-coordinates of points in the green circle are near to normal according to the histograms.

From Figure 8b, it is known that $\left(\theta_{t\_tn}, \dot{\theta}_{t\_stn}\right) \in D_{\omega_m,\varphi_j}$ correspond to a two-dimensional Gaussian distribution $N_{t|\omega_m,\varphi_j}(\boldsymbol{\mu}, \boldsymbol{\Sigma})$. For each $N_{t|\omega_m,\varphi_j}(\boldsymbol{\mu}, \boldsymbol{\Sigma})$, it can be calculated as:

$$
\begin{gathered}
\boldsymbol{\mu} = \begin{bmatrix}\mu_1\\ \mu_2\end{bmatrix}, \boldsymbol{\Sigma} = \begin{bmatrix}Cov(X_1,X_1) & Cov(X_1,X_2)\\ Cov(X_2,X_1) & Cov(X_2,X_2)\end{bmatrix}\\
\mu_1 = \Big(\sum_{D_{\omega_m,\varphi_j}} \theta_{t\_tn}\Big)/\left|D_{\omega_m,\varphi_j}\right|, \mu_2 = \Big(\sum_{D_{\omega_m,\varphi_j}} \dot{\theta}_{t\_stn}\Big)/\left|D_{\omega_m,\varphi_j}\right|\\
Cov(X_1,X_1) = \sum_{D_{\omega_m,\varphi_j}} (\theta_{t\_tn} - \mu_1)^2 / \left(\left|D_{\omega_m,\varphi_j}\right| - 1\right)\\
Cov(X_2,X_2) = \sum_{D_{\omega_m,\varphi_j}} (\dot{\theta}_{t\_stn} - \mu_2)^2 / \left(\left|D_{\omega_m,\varphi_j}\right| - 1\right)\\
Cov(X_1,X_2) = Cov(X_2,X_1) = \sum_{D_{\omega_m,\varphi_j}} (\theta_{t\_tn} - \mu_1)(\dot{\theta}_{t\_stn} - \mu_2) / \left(\left|D_{\omega_m,\varphi_j}\right| - 1\right)
\end{gathered} \tag{12}
$$

f_p Gaussian distributions from $N_{t|\omega_m,\varphi_0}(\boldsymbol{\mu},\boldsymbol{\Sigma})$ to $N_{t\ |\omega_m,\varphi_{f_p-1}}(\boldsymbol{\mu},\boldsymbol{\Sigma})$ together represent the TPDS under ω_m mode. TPDSs in different locomotion modes are shown in Figure 9a.

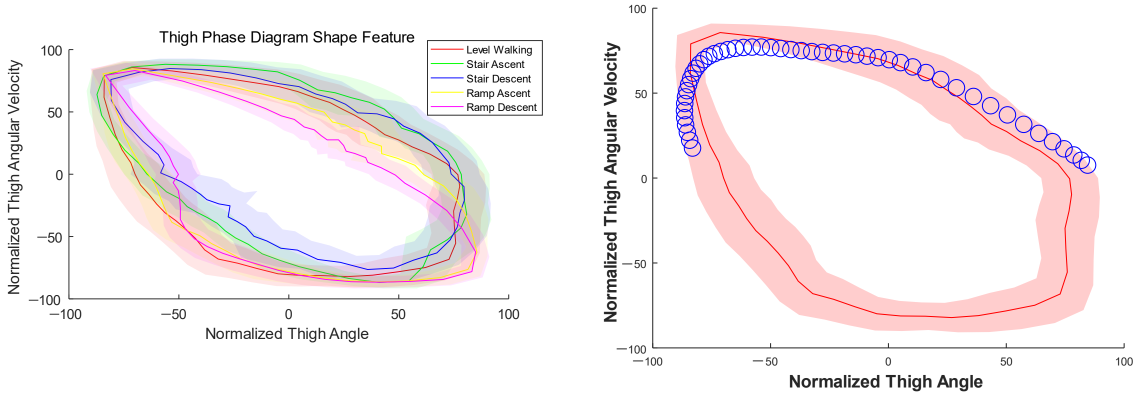

(**a**) (**b**)

Figure 9. (**a**) TPDSs in different locomotion modes. The solid line is the mean trajectory, and the transparent area is ±1 standard deviation. (**b**) The red part is the standard TPDS of LW mode. Blue points form the real-time thigh phase diagram trajectory, and the blue points are collected under LW mode.

The overlap degree between real-time thigh phase diagram trajectory and standard TPDSs of different modes shown in Figure 9b is an index of similarity to classify locomotion modes. The summation of the probability density of each sample point is used to evaluate the overlap degree:

$$sum_{t|\omega_m}(t) = \sum_{k=0}^{L_{tw}-1} f_{t|\omega_m,\varphi_j}(\theta_{t\_tn}(t-k\cdot t_s), \dot{\theta}_{t\_stn}(t-k\cdot t_s)) \tag{13}$$

where $f_{t|\omega_m,\varphi_j}(x,y)$ is the probability density function of $N_{t|\omega_m,\varphi_j}(\boldsymbol{\mu},\boldsymbol{\Sigma})$. Then we can figure out the conditional probability, $P(\omega_m|TPDS(t))$, of each mode:

$$P(\omega_m \Big| TPDS(t)) = sum_{t|\omega_m}(t) / \sum_{i=1}^{M} sum_{t|\omega_i}(t) \tag{14}$$

where $TPDS(t)$ represents the TPDS feature at time t.

2.2.2. Knee Angle Trajectory (KAT)

KAT is the normalized knee angle trajectory at the gait phase axis. Similarly to TPDS, $\theta_{k\_sn} \in D_{\omega_m,\varphi_j}$ correspond to a one-dimensional normal distribution $N_{k|\omega_m,\varphi_j}(\mu,\Sigma)$. Standard KATs in different locomotion modes are shown in Figure 10.

The summation of probability density is used to evaluate the overlap degree of real-time KAT and the standard KAT under ω_m mode:

$$sum_{k|\omega_m}(t) = \sum_{k=0}^{L_{tw}-1} f_{k|\omega_m,\varphi_j}(\theta_{k\_sn}(t-k\cdot t_s)) \tag{15}$$

where $f_{k|\omega_m,\varphi_j}(x)$ is the probability density function of $N_{k|\omega_m,\varphi_j}(\mu,\Sigma)$. The conditional probability $P(\omega_m|KAT(t))$ of each mode is:

$$P(\omega_m \Big| KAT(t)) = sum_{k|\omega_m}(t) / \sum_{i=1}^{M} sum_{k|\omega_i}(t) \tag{16}$$

where $KAT(t)$ represents the KAT feature at time t.

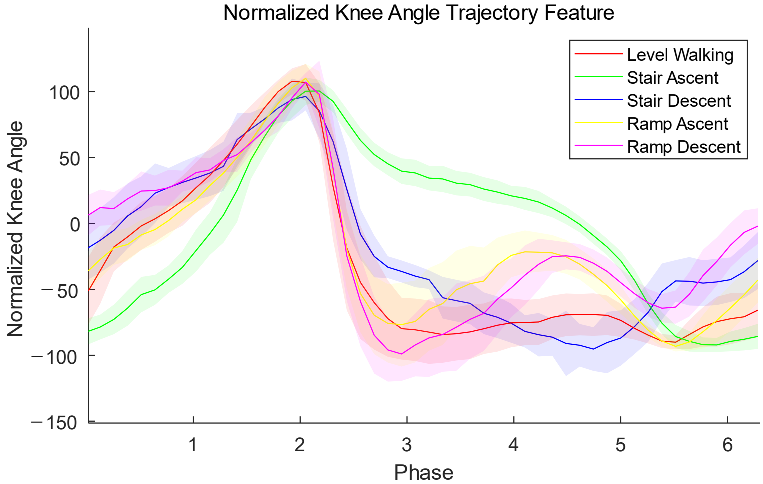

Figure 10. KATs in different locomotion modes. The x-axis is the continuous thigh phase variable $\varphi_{new}(t)$ which represents a whole gait cycle, and the y-axis is the normalized knee angle $\theta_{k\_sn}(t)$. The solid line is the mean trajectory, and the transparent area is ± 1 standard deviation.

2.2.3. Center Position Offset (CPO)

During the translation of the thigh phase diagram in Equation (7), the translation vector (β_x, β_y) can reflect the range of thigh motion. The translation vector is called CPO. In different locomotion modes, the distributions of $(\beta_x, \beta_y) \in D_{\omega_m}$ are shown in Figure 11a. The two-dimensional normal distribution function $N_{c|\omega_m}(\boldsymbol{\mu}, \boldsymbol{\Sigma})$ is used to describe CPO under ω_m mode. The probability density function of $N_{c|\omega_m}(\boldsymbol{\mu}, \boldsymbol{\Sigma})$ is $f_{c|\omega_m}(x, y)$, and the conditional probability under CPO is

$$P(\omega_m|CPO(t)) = f_{c|\omega_m}(\beta_x(t), \beta_y(t)) / \sum_{i=1}^{M} f_{c|\omega_i}(\beta_x(t), \beta_y(t)) \tag{17}$$

where $CPO(t)$ represents the CPO feature at time t.

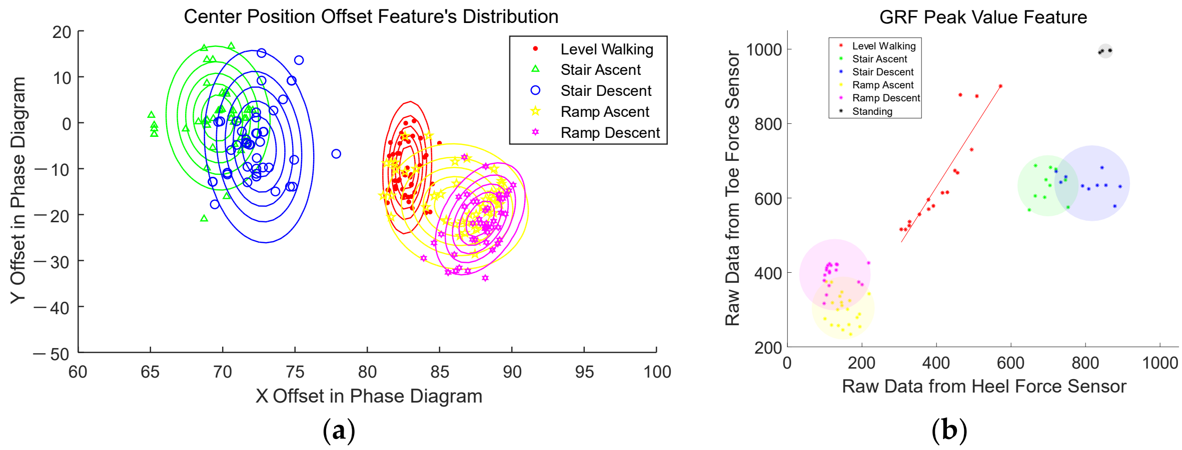

Figure 11. (**a**) CPO distributions in different modes. Ellipses represent probability density contours, and the points represent the translation vector (β_x, β_y) in different modes. (**b**) GRFPV feature distributions in different modes. Points represent parts of sample points (G_{hp}, G_{tp}). The line segment is fitted by points of D_{LW}. The circles contain all sample points of one mode with the smallest radius.

2.2.4. Ground Reaction Force Peak Value (GRFPV)

The peak values of the force and heel force have different distributions in different locomotion modes, as shown in Figure 11b. We assume that the GRFPV of LW are assembling near a line segment and GRFPV of other modes are gathering in a circle.

The line segment AB is fitted by the least square method:

$$a_{\omega_m}x + b_{\omega_m}y + c_{\omega_m} = 0, x_A \le x \le x_B, \omega_m = \mathrm{LW} \tag{18}$$

The coordinate of each circle center of each mode is

$$C_{\omega_m}\left(x_{\omega_m},\ y_{\omega_m}\right),\ \omega_m\ \ne\ \mathrm{LW} \tag{19}$$

Then Euclidean distance is used to compute the relative probability RP_{ω_m}:

$$RP_{\omega_m} = \frac{3}{1 + 2 * \exp(d/100)} \tag{20}$$

where d is

$$d = \begin{cases} |pA| & \angle pAB > 90^\circ & \\ |pB| & \angle pBA > 90^\circ & \omega_m = LW \\ \frac{|a_{\omega_m}G_{hp}(t) + b_{\omega_m}G_{tp}(t) + c_{\omega_m}|}{\sqrt{a_{\omega_m}^2 + b_{\omega_m}^2}} & else & \\ |pC_{\omega_m}| & & \omega_m \ne LW \end{cases} \tag{21}$$

where $p(G_{hp}(t),\ G_{tp}(t))$ is the GRFPV point in real time. The conditional probability $P(\omega_m|GRFPV(t))$ is:

$$P(\omega_m \Big| GRFPV(t)) = RP_{\omega_m} / \sum_{i=1}^{M} RP_{\omega_m} \tag{22}$$

where $GRFPV(t)$ represents the GRFPV feature at time t.

It should be noted that ST is not periodic movement and does not have a stable phase variable. The TPDS, KAT, and CPO features of ST are not calculated.

3. Results

The workflow of real-time feature extraction and classification is shown in Figure 12. This paper designs two classifiers: the standing (ST) classifier is used to identify the ST mode, and the artificial neural network (ANN) classifier is used to classify the other five locomotion modes.

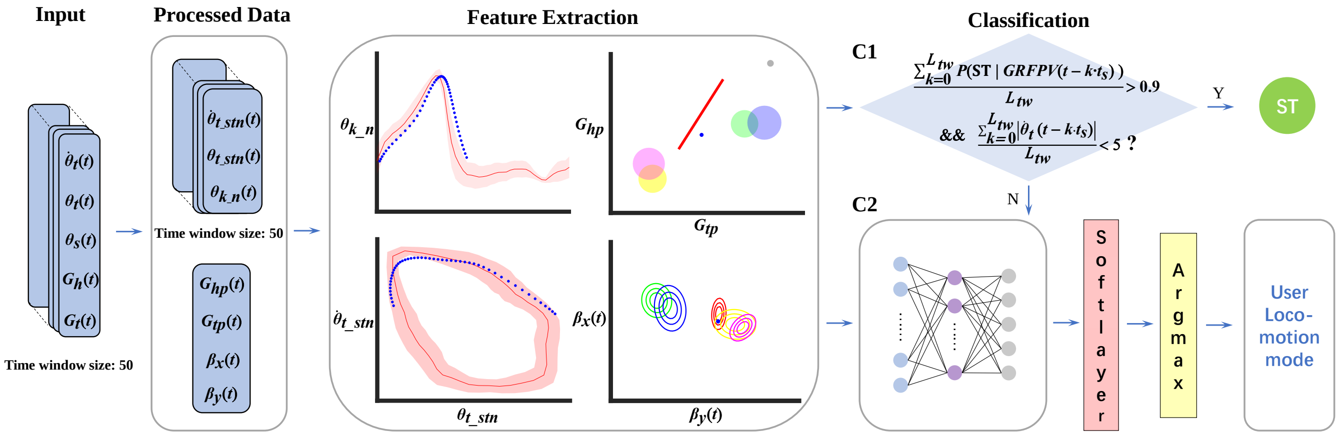

Figure 12. Real-time feature extraction and classification. C1 is the standing (ST) classifier, and C2 is the artificial neural network (ANN) classifier. The blue points are real-time feature points under LW.

3.1. ST Classifier

An angular velocity threshold and GRFPV feature are used at the ST classifier, as shown in Figure 12. The threshold Th satisfies

$$DT = \sum_{k=0}^{L_{tw}} \left| \dot{\theta}_t(t - k \cdot t_s) \right| / L_{tw} < Th \tag{23}$$

where DT is the dynamic trend. When the subject is standing, the DT curve is shown in Figure 13a, and the maximum DT is smaller than 2. Then, 10,000 sample points are randomly sampled in other modes, and their DT distribution is shown in Figure 13b. The minimum DT under other modes is greater than 7. Here, we take $Th = 5$.

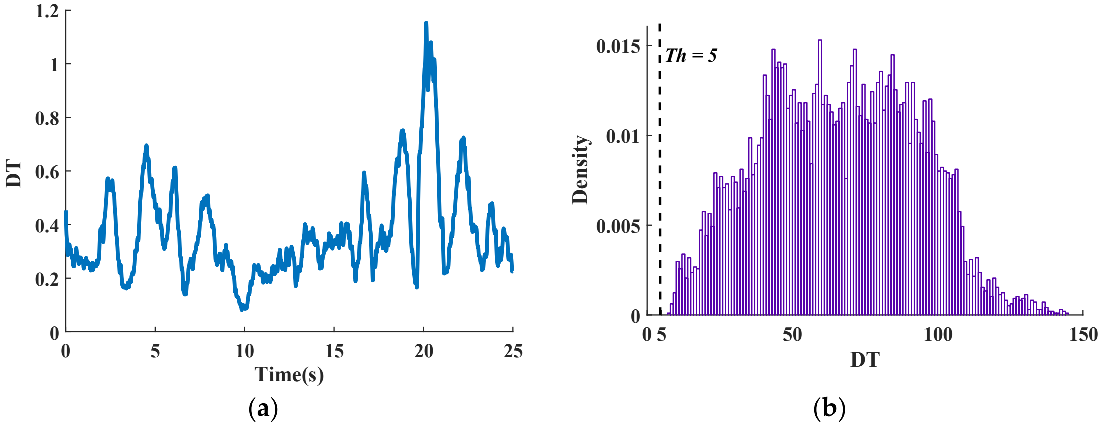

Figure 13. (**a**) The dynamic trend under ST mode. (**b**) Ten thousand sample points are randomly sampled in other modes, and their DT distribution is shown above.

The threshold ensures that there won't be much movement, while the GRFPV feature inequality ensures that the subject is standing on the ground. The ST classifier has an accuracy of 100% in the test because standing has an obvious static feature which is different from periodic locomotion modes.

3.2. ANN Classifier

At the ANN classifier, the conditional probabilities of each mode under each feature are input into a fully connected neural network with one hidden layer, as shown in Figure 14, and the final outputs are the probabilities of each locomotion mode. The calculations of the hidden layer and output layer are shown in Equation (24).

$$y_j = g\left(\sum_{i=1}^{4M} \omega_{ij}^{l1} \cdot x_i + b_j^{l1}\right), z_j = \mathrm{g}\left(\sum_{i=1}^{H} \omega_{ij}^{l2} \cdot y_i + b_j^{l2}\right) \tag{24}$$

where $\omega_{\mathrm{ij}}^{l1}$ and b_j^{l1} are the weight matrix and bias between input and hidden layer. $\omega_{\mathrm{ij}}^{l2}$ and b_j^{l2} are the weight matrix and bias between the hidden and output layers. g is the tansig function. During the training process, the training dataset and validation dataset are strictly separated.

The data was trained on a particular subject, and the ANN classifier was evaluated by a five-fold cross-validation. The testing results of eight subjects are listed in Table 2 below, and the confusion matrix of eight subjects is shown in Table 3. The ANN classifier has an average accuracy across all subjects of 99.16% ± 0.38%.

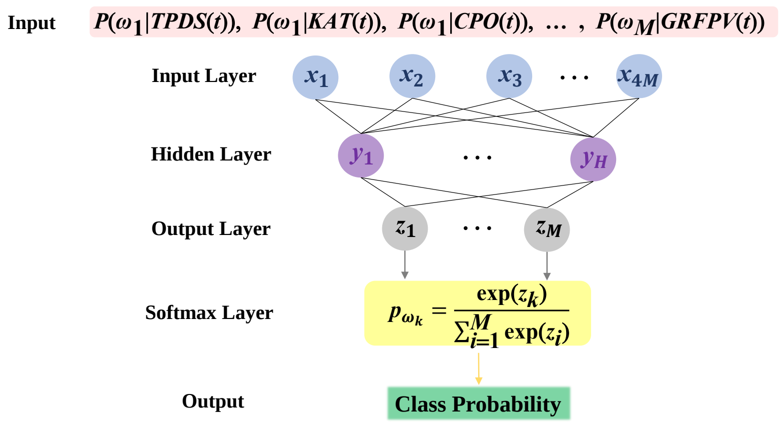

Figure 14. The structure of the designed neural network.

Table 2. Classification results for 8 Subjects.

Testing Accuracy		**Locomotion Modes**					
		LW	**SA**	**SD**	**RA**	**RD**	**Total**
Subjects M = Man W = Woman	M1	100.0	99.89	99.08	99.10	98.71	99.36
	M2	100.0	99.67	99.90	97.55	97.59	98.94
	M3	100.0	99.71	99.11	98.88	98.65	99.27
	M4	100.0	99.15	99.19	97.73	97.32	98.68
	M5	99.99	99.89	99.39	97.36	96.90	98.71
	M6	**100.0**	**100.0**	**99.59**	**99.33**	**99.58**	**99.70**
	W1	100.0	98.69	99.53	100.0	99.63	99.57
	W2	99.94	98.48	98.85	99.16	98.75	99.04

Table 3. The confusion matrix of the accuracy tests.

Confusion Matrix		**Predicted Class**					
		LW	**SA**	**SD**	**RA**	**RD**	**None**
Actual Class	LW	99.99				0.01	
	SA		99.44	0.56			
	SD		0.67	99.33			
	RA		0.05		98.64	1.30	0.01
	RD				1.61	98.38	0.01

Compared with the traditional confusion matrix, we add one column of "None" to represent the unclassified mode when

$$\max(p_{\omega_k}) < 0.5, k = 1, 2, \ldots, M \tag{25}$$

4. Discussion

4.1. Network Hyperparameters

The performance of ANN is closely related to the network structure. Here, the following hyperparameters are considered: (1) the number of neurons in the hidden layer (N_{hidden}); (2) the number of groups of training data for each mode (N_{train}) in the training set. N_{hidden} affects network structure and N_{train} may lead to overfitting or underfitting. Based on M1′s user-dependent dataset, tests are carried out under different parameters, and the results are shown in Figure 15a. The bigger N_{train} corresponds to higher classification accuracy. However, classification accuracy has already reached 95% when $N_{train} = 200$, which shows that the proposed method can achieve good results when training with a small amount of data. When $N_{train} = 2000$ and $N_{hidden} = 25$, we get the best classification accuracy of M1.

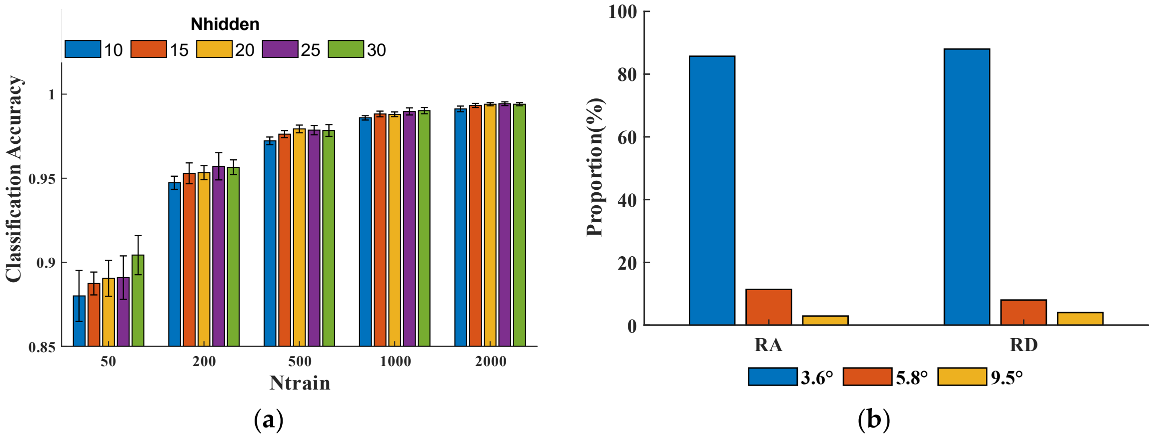

Figure 15. (**a**) Classification accuracy under different N_{hidden} and N_{train}. The error bar represents ±1 standard deviation. (**b**) Error's proportion of different slopes under RA and RD.

4.2. Ramp Slope

From Tables 2 and 3, classification errors mainly focus on RA and RD. The proportion of each error of different slopes in the whole error under RA and RD is shown in Figure 15b. The result shows that the main error occurs in the low slopes, which indicates that gaits under low slopes have similarities.

4.3. Time Window Length

Time window size decides how much information we can use when classification is in progress. However, the bigger time window size will bring higher delay. Based on M1′s user-dependent dataset, we test the average accuracy under different time window sizes when N_{train}= 2000 and $N_{hidden} = 25$. The result is shown in Figure 16. When the time window size reaches 50, the classification accuracy increases very slowly.

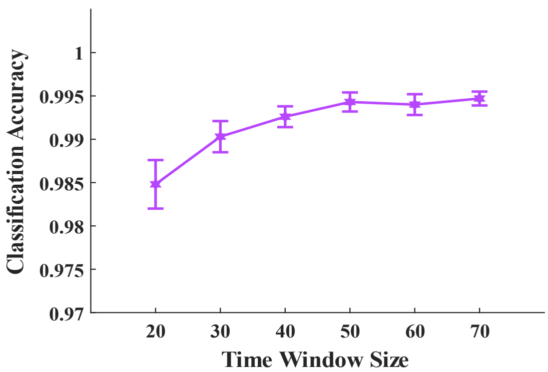

Figure 16. Classification accuracy under different time window sizes. Error bars represent ±1 standard deviation.

5. Conclusions

The high accuracy of locomotion mode classification ensures prosthetic users' safety and are the foundation of the natural transition between locomotion modes. In this paper, four novel features are proposed based on data from two IMUs and one GRF insole. Gaussian distributions are used to describe the TPDS, KAT and CPO features after using distribution fitter tools to analyze the data. Euclidean distances in GRFPV diagrams are used to compute the relative probabilities of different locomotion modes. To the author's knowledge, those features haven't been proposed and applied yet. ST classifier and ANN classifier are designed and achieve a high accuracy of 100% and 99.16% $\pm$ 0.38%, respectively.

Moreover, the proposed method is potential for future research. The real-time classified walking data are used to adjust features' distribution to adapt amputee's gaits. The new extracted feature is convenient to be added to our control framework. The ANN used in this paper is simple in structure, which makes it possible to train ANN online. Additionally, human locomotion modes are not limited to the listed. When the predicted class is "None," we can collect the unclassified data and apply clustering algorithms to discover new modes. Those evolutionary and adaptive abilities are what we will study next.

To further our study, the disabled volunteers will be invited to test the proposed method. Except for locomotion mode classification, more information such as slopes, step stride and stair height will be predicted by analyzing the walking dataset.

Author Contributions: Conceptualization, Y.L. and H.A.; methodology, Y.L. and H.A.; software, Y.L.; validation, Y.L., H.A. and H.M.; formal analysis, Y.L.; data curation, Y.L.; writing—original draft preparation, Y.L.; writing—review and editing, H.A., H.M. and Q.W.; visualization, Y.L.; supervision, H.A., H.M. and Q.W.; project administration, H.A.; funding acquisition, H.A., H.M. and Q.W. All authors have read and agreed to the published version of the manuscript.

Funding: This research was funded by the project of the National Key Research and Development Program of China, grant number (2018YFC2001304).

Informed Consent Statement: Not applicable.

Data Availability Statement: Not applicable.

Conflicts of Interest: The authors declare no conflict of interest.

Appendix A

Abbreviations in this paper are shown in Table A1.

Table A1. Abbreviations in this paper.

Abbreviations	Full Names	Abbreviations	Full Names
LW	level walking	SA	stair ascent
SD	stair descent	RA	ramp ascent
RD	ramp descent	ST	standing
TPDS	thigh phase diagram shape	KAT	knee angle trajectory
CPO	center position offset	GRFPV	ground reaction force peak value
ANN	artificial neural network	WHO	world health organization
LLA	lower-limb amputation	PR	pattern recognition
ML	machine learning	sEMG	surface electromyogram
EFRS	environmental feature recognition system	LDA	linear discriminant analysis
QDA	quadratic discriminant analysis	GMM	Gaussian mixture model
DBN	dynamic Bayesian network	IMU	inertial measurement unit
GRF	ground reaction force	CNN	convolutional neural network
DL-based	deep learning based	LG	level ground
M	man	W	woman
DT	dynamic trend		

References

1. Filmer, D. Disability, Poverty, and Schooling in Developing Countries. *Soc. Sci. Electron. Publ. Vol.* **2008**, *22*, 141–163.
2. Au, S.K.; Weber, J.; Herr, H.M. Powered Ankle—Foot Prosthesis Improves Walking Metabolic Economy. *IEEE Trans. Robot.* **2009**, *25*, 51–66. [CrossRef]
3. Wang, Q.N.; Zheng, E.H.; Chen, B.J.; Mai, J.G. Recent Progress and Challenges of Robotic Lower-limb Prostheses for Human-robot Integration. *Acta Autom. Sin.* **2016**, *42*, 1780–1793.
4. Tucker, M.R.; Olivier, J.; Pagel, A.; Bleuler, H.; Bouri, M.; Lambercy, O.; Gassert, R. Control strategies for active lower extremity prosthetics and orthotics: A review. *J. NeuroEngineering Rehabil.* **2015**, *12*, 1–30. [CrossRef] [PubMed]

5. Fleming, A.; Stafford, N.; Huang, S.; Hu, X.; Ferris, D.P.; Huang, H.H. Myoelectric control of robotic lower limb prostheses: A review of electromyography interfaces, control paradigms, challenges and future directions. *J. Neural Eng.* **2021**, *18*, 041004. [CrossRef] [PubMed]
6. Simao, M.; Mendes, N.; Gibaru, O.; Neto, P. A Review on Electromyography Decoding and Pattern Recognition for Human-Machine Interaction. *IEEE Access* **2019**, *7*, 39564–39582. [CrossRef]
7. Spanias, J.A.; Simon, A.M.; Finucane, S.B.; Perreault, E.J.; Hargrove, L.J. Online adaptive neural control of a robotic lower limb prosthesis. *J. Neural Eng.* **2018**, *15*, 016015. [CrossRef] [PubMed]
8. Zhang, K.; Xiong, C.; Zhang, W.; Liu, H.; Lai, D.; Rong, Y.; Fu, C. Environmental Features Recognition for Lower Limb Prostheses Toward Predictive Walking. *IEEE Trans. Neural Syst. Rehabil. Eng.* **2019**, *27*, 465–476. [CrossRef] [PubMed]
9. Young, A.J.; Simon, A.M.; Fey, N.P.; Hargrove, L.J. Classifying the intent of novel users during human locomotion using powered lower limb prostheses. In Proceedings of the 2013 6th International IEEE/EMBS Conference on Neural Engineering (NER), San Diego, CA, USA, 6–8 November 2013; IEEE: Piscataway, NJ, USA, 2013; pp. 311–314.
10. Ha, K.H.; Varol, H.A.; Goldfarb, M. Volitional Control of a Prosthetic Knee Using Surface Electromyography. *IEEE Trans. Biomed. Eng.* **2010**, *58*, 144–151. [CrossRef] [PubMed]
11. Varol, H.A.; Sup, F.; Goldfarb, M. Multiclass Real-Time Intent Recognition of a Powered Lower Limb Prosthesis. *IEEE Trans. Biomed. Eng.* **2009**, *57*, 542–551. [CrossRef] [PubMed]
12. Huang, H.; Zhang, F.; Hargrove, L.J.; Dou, Z.; Rogers, D.R.; Englehart, K.B. Continuous Locomotion-Mode Identification for Prosthetic Legs Based on Neuromuscular-Mechanical Fusion. *IEEE Trans. Biomed. Eng.* **2011**, *58*, 2867–2875. [CrossRef] [PubMed]
13. Young, A.J.; Simon, A.M.; Fey, N.P.; Hargrove, L.J. Intent Recognition in a Powered Lower Limb Prosthesis Using Time History Information. *Ann. Biomed. Eng.* **2013**, *42*, 631–641. [CrossRef] [PubMed]
14. Samuel, A.; Berniker, M.; Herr, H. Powered ankle-foot prosthesis to assist level-ground and stair-descent gaits. *Neural Netw. Off. J. Int. Neural Netw. Soc.* **2008**, *21*, 654–666.
15. Su, B.Y.; Wang, J.; Liu, S.Q.; Sheng, M.; Jiang, J.; Xiang, K. A CNN-Based Method for Intent Recognition Using Inertial Measurement Units and Intelligent Lower Limb Prosthesis. *IEEE Trans. Neural Syst. Rehabil. Eng.* **2019**, *27*, 1032–1042. [CrossRef] [PubMed]
16. Kang, I.; Molinaro, D.D.; Choi, G.; Camargo, J.; Young, A.J. Subject-Independent Continuous Locomotion Mode Classification for Robotic Hip Exoskeleton Applications. *IEEE Trans. Biomed. Eng.* **2022**, *69*, 3234–3242. [CrossRef] [PubMed]
17. Bhakta, K.; Camargo, J.; Donovan, L.; Herrin, K.; Young, A. Machine learning model comparisons of user independent & dependent intent recognition systems for powered prostheses. *IEEE Robot. Automat. Lett.* **2020**, *5*, 5393–5400.
18. Lawson, B.E.; Mitchell, J.; Truex, D.; Shultz, A.; Ledoux, E.; Goldfarb, M. A robotic leg prosthesis: Design, control, and implementation. *IEEE Robot. Autom. Mag.* **2014**, *21*, 70–81. [CrossRef]
19. Quintero, D.; Lambert, D.J.; Villarreal, D.J.; Gregg, R.D. Real-time continuous gait phase and speed estimation from a single sensor. In Proceedings of the 2017 IEEE Conference on Control Technology and Applications (CCTA), Kohala Coast, HI, USA, 27–30 August 2017; IEEE: Piscataway, NJ, USA, 2017; pp. 847–852.